

Experimental and numerical investigation of effects of premixing on soot processes in *iso*-octane co-flow flames.

A. Makwana, A. Jain, M. Linevsky, S. Iyer, R. Santoro, T. Litzinger, Y. Xuan, J. O'Connor*

Mechanical and Nuclear Engineering, Pennsylvania State University, University Park, PA, USA

*Corresponding author

Address: 111 Research East Building, University Park, PA 16802

Email: jxo22@engr.psu.edu

- **Colloquium**: SOOT, NANOMATERIALS, AND LARGE MOLECULES
- **Alternate Colloquium**: LAMINAR FLAMES
- Total length of the paper (Method 1): 6200

	Words
Main text	4104
Nomenclature	0
References	576
Figure 1	367
Figure 2	201
Figure 3	214
Figure 4	199
Table 1	167
Table 2	288
Equations	84
Total	6200

- We do not need a color print for the paper.

Abstract

The goal of the current work is to understand the effects of premixing on soot processes in an *iso*-octane, axisymmetric, co-flow, laminar flame at atmospheric pressure. The flames investigated are non-premixed and partially-premixed (jet equivalence ratios of 24, 15, 12, 9 and 6). The total carbon flow rate is kept constant to facilitate comparison among the six flames. Laser-induced incandescence and laser extinction are applied to obtain two-dimensional soot volume fraction. The experimental results show that the spatial distribution of soot changes with premixing; the peak soot volume fraction location is in the annular region in the non-premixed flame and transitions to the centerline as the jet equivalence ratio is reduced. Numerical simulations are performed using a detailed *iso*-octane fuel chemistry and tri-variate soot model. The numerical model captures the changes in the spatial distribution of soot due to premixing, as in the experiment. Similar to the change in the soot distribution, the soot production processes, including nucleation, surface growth, and PAH condensation, show the transition behavior with premixing. The simulation shows that the location of peak PAH dimer concentration shifts from the annular region towards the centerline with premixing. As a result, the location where soot nucleation and PAH condensation rates peak show similar transition as observed in the PAH dimer concentration. Furthermore, PAH dimer concentration decreases due to premixing, leading to a decrease in the soot nucleation and soot growth due to PAH condensation. Additionally, soot growth due to surface reactions decrease with premixing due to the reduction in number of active sites on the soot surface.

Keywords: *iso*-octane, soot, premixing, environmental aspects.

1. Introduction

The present study expands on our previous work where we experimentally investigated the effects of fuel molecular structure on emissions [1, 2]. In that work [1, 2], we found that *iso*-octane/*n*-dodecane (iC8) and methycyclohexane/*n*-dodecane (MCH) fuel blends had the highest sooting propensity amongst several paraffin fuels: *n*-heptane/*n*-dodecane, *n*-dodecane and *n*-hexadecane/*n*-dodecane. The iC8 and MCH fuels also displayed an interesting feature with premixing, where the location of the peak soot transitioned from the annular region to the centerline as the level of premixing increased. The transition occurs at jet equivalence ratios (ϕ_{jet}) between infinity (non-premixed) and 24. In the present study, we explore the physical and chemical processes responsible for this trend in peak soot by considering *iso*-octane flames at a range of jet equivalence ratios, using both experimental and numerical methods. *iso*-Octane is an important molecule to study because it is a primary reference fuel, and it is used to represent *iso*-alkane components of real fuels in surrogate fuel formations [3, 4].

A number of studies in co-flow flames have investigated soot experimentally and utilized the data to validate chemical-kinetic and soot models; past studies have mostly focused on gaseous fuels [5] or gaseous fuels doped with higher hydrocarbon fuels [6, 7]. Studies reporting both experimental and numerical investigation of soot formation from neat high molecular weight fuels are limited. The use of high molecular weight fuels is a step towards understanding soot formation from real transportation fuels. Soot formation studies specifically involving *iso*-octane fuel are limited. Frenzel *et al.* [8] investigated the effects of ethanol and butanol on an *iso*-octane flame in a McKenna burner. Zeng *et al.* [9] investigated the influence of dimethyl ether and diethyl ether addition on flame structure and pollutants in an premixed *iso*-octane flame. However, experimental data for soot volume fraction (f_v) under both non-premixed and premixed condition for *iso*-octane fuel remains scarce. To the best of authors' knowledge, the present study represents the first study providing experimental and modeling results for f_v under both premixed and partially-premixed conditions for *iso*-octane in a co-flow flame configuration.

Variations in the peak soot location have been reported in ethylene flames. Santoro *et al.* [10] observed the peak soot transition behavior when the fuel-jet velocity was increased. Smooke *et al.* [5] observed the transition of the peak soot location from the annular region to the centerline when nitrogen dilution in the fuel jet was increased. These authors posited that the increase in dilution resulted in a decrease in the residence time of soot in the wings. Also, the relative importance of soot inception and growth processes change with dilution. In contrast to previous studies involving the transition behavior, the presence of oxygen in the current study could also have chemical effects on soot formation processes. Chernov *et al.* [11] numerically investigated the effects of premixing on soot in ethylene flames. The authors found that soot growth on the flame centerline is due to both PAH and acetylene processes. However, in the annular region, acetylene addition dominated the soot mass yield.

The goal of the current work is to understand the processes controlling the transition of peak soot location in a laminar, co-flow flame for a high-hydrocarbon fuel that is representative of fuel components in real transportation fuels. In particular, we are interested in understanding the relative roles of gas-phase vs. condensed-phase processes in controlling the soot distribution. To derive this understanding, we use a combination of experimental measurements and numerical methods with detailed chemistry and soot models. The intent of using simulation was to understand the physics of the processes responsible for the trends in f_v due to premixing for a high molecular weight fuel, observed experimentally. The soot model has already been validated for gaseous fuels [12-14].

2. Methods/Experimental

2.1 Burner system

The co-annular burner used in this study is a modified version of the burner used by Santoro *et al.* [10]. The burner consists of two concentric brass tubes, where the outer air tube has a 101.6 mm diameter. The inner fuel tube diameter is 11.1 mm and this tube protrudes 4 mm above the plane of the co-flow. A detailed description of the burner system is in Ref. [1]. The fuel is supplied using an Isco 500D syringe pump (rated flow rate accuracy $\pm 0.5\%$) to the vaporization chamber. The energy for fuel vaporization is

provided by heating tapes that are wrapped around the vaporization chamber. The temperature of the heating tapes is maintained at 150 °C in order to vaporize and prevent condensation of the fuel. Gas chromatography is used on the fuel at the exit of burner tube to ensure that no fuel pyrolysis has occurred in the tubing system.

2.2 Diagnostic methods

The two-dimensional soot volume fraction (f_v) is obtained using laser induced incandescence (LII). The optical setup, data collection, analysis, and measurement uncertainties of the setup are identical to our previous work [1]. In LII [15], the laser beam from a Nd:YAG laser (Spectra Physics GCR 270-10, 10Hz, 7 ns, 532 nm) is expanded to a laser sheet by use of a plano-convex cylindrical lens and focused on the center of the burner using a convex lens. At a laser fluence of 0.3 J/cm², the 22.5 mm laser sheet was found to be in plateau region of LII. The LII signal from soot is collected by a Princeton Instruments ICCD camera with a filter centered at 430 nm with 10 nm FWHM and an f 2.8, 105mm UV lens. The camera is gated for 100 ns after an initial delay of 20 ns after the laser pulse. The LII signal is corrected for background noise, pixel-to-pixel responsivity of the detector, and non-uniformity in the laser intensity using an identical procedure to that described in Ref. [1]. The LII signals are calibrated using laser extinction (LE); the calibration factor of 3350 counts is equivalent to 1 ppm of soot. The estimated uncertainty of f_v associated with LE and LII is $\pm 15\%$. An argon-ion laser (Coherent Innova 70) at a 514.5 nm wavelength is used for the LE experiment. A value of $\tilde{m} = 1.57 - 0.56i$ is used as refractive index of soot to be consistent with our published work [1]. The line-of-sight extinction results are deconvoluted using a Fourier inversion technique [16].

2.3 Experimental Conditions

The experimental matrix is provided in Table 1. The flames studied are non-premixed and partially-premixed flames. The carbon flow rate of fuel is kept constant for all the flames at 0.0111 mol/min, to be consistent with our previous work [1]. The vaporized fuel is carried from the vaporization chamber to the tube exit using a 200 cm³/min stream of nitrogen. The co-flow air is set at 0.113 m³/min.

The purity level of *iso*-octane used in the experiment is > 99%. In the simulation, the fuel inlet temperature, 650 K, is measured experimentally using an R-type thermocouple. The methodology to obtain temperature measurements is discussed in Ref. [1] and the measurements are provided in the supplementary material. The temperature of co-flow air is 323 K.

Table 1. Matrix of fuel mixtures

Liquid Fuel flow rate (ml/min)	Equivalence ratio (ϕ_{jet})	Carbon flow rate [mol/min]	Study	Model boundary condition	
				Fuel velocity [cm/s]	Fuel temperature (K)
0.23	∞	0.0111	Exp + Num	9.06	650
	24		Exp + Num	12.39	
	15		Exp	-	
	12		Exp + Num	15.64	
	9		Exp	-	
	6		Exp + Num	22.16	

2.4 Simulation description

2.4.1 Simulation Framework

The flow solver used in this work is the NGA code [17]. The equations for conservation of mass, momentum, species, and energy are solved using a finite difference formulation in cylindrical coordinates. The BQUICK scheme is used for solving the discretized species and temperature equations. This scheme ensures that the transported scalars remain within their physical bounds [18]. A recently-developed computationally-efficient, semi-implicit, iterative method is used for the time integration of the chemical source terms in the transport equations of gas-phase species. This method has been shown to be free of lagging errors, as efficient as an explicit time-integration per time step, and capable of using large, stable

time-step sizes [19]. These numerical methods guarantee globally second-order accuracy in both space and time [20].

The detailed chemistry model employed in the current work contains 185 species and 1903 reactions (forward and backward reactions counted separately), and takes into account all major pathways of polycyclic aromatic hydrocarbons (PAH) formation [20]. A recent study [21] has found that the pyrene mass fraction is under predicted, using this chemistry model, as compared to the experiment in a *n*-heptane laminar premixed flame. However, the predictions of benzene, naphthalene, and phenanthrene were within the experimental uncertainties. The under-prediction of pyrene may affect the prediction of f_v ; however, the trends visible in f_v due to premixing are expected to hold. This chemical model has been extensively validated for multiple fuels [22], including the one used in this study. This model has been used in multiple configurations, including laminar and turbulent flames [13, 23].

2.4.2. Soot Model

The soot model employed in the current study is taken from Ref. [14], which is a simplified version of that presented in Ref. [24]. Soot particles are considered as fractal aggregates and geometrically described based on the total volume, V , and total surface area, S . The population of the soot particles is statistically described using a bi-variate soot Number Density Function (NDF), $n(V; S)$, and is approximated by two delta functions, following previous work [20]. The evolution of soot is determined by transporting key soot moments

$$M_{x,y} = \iint n(V, S) V^x S^y dV dS \quad (1)$$

of the soot NDF using the following transport equation

$$\frac{\partial M_{x,y}}{\partial t} + \nabla \cdot (\mathbf{u}^* M_{x,y}) = \dot{\omega}_{x,y} \quad (2)$$

where

$$\mathbf{u}^* = \mathbf{u} - 0.556(\nu/T)\nabla T \quad (3)$$

is the velocity vector accounting for thermophoresis effects [25, 26], ν is fluid kinematic viscosity, and $\dot{\omega}_{x,y}$ accounts for the various contributions from soot nucleation, condensation, surface growth, and

oxidation [24]. The soot model has been validated for gaseous fuels at both non-premixed and premixed conditions [12, 13].

3. Results and Discussion

3.1 Visible flame heights.

Figure 1 shows the experimental and numerical results of the soot volume fraction obtained for *iso*-octane flames at $\phi_{\text{jet}} = \infty, 24, 12$ and 6 conditions. The numerical study is carried out for these four flame conditions as they represent the observed sooting behavior, and therefore, results for $\phi_{\text{jet}} = 15$ and 9 are not presented in Fig. 1. In the experimental results, the flame heights, as defined by the visible flame images, are approximately 65 mm, 58 mm, 55 mm and 50 mm, for $\phi_{\text{jet}} = \infty, 24, 12$ and 6 conditions, respectively. The flame height uncertainty is ± 2 mm. Long-exposure images of the flames, obtained using a commercial camera, show that the visible blue flame is separated from the fuel tube exit by approximately 1 mm. In the simulation, the flame height is equivalent to the distance from the tube exit to the tip of the $f_v = 0.1$ ppm isocontour. The flame heights from the simulation are 58 mm, 49 mm, 48 mm, and 43 mm for $\phi_{\text{jet}} = \infty, 24, 12,$ and 6 conditions, respectively. In both the experimental and numerical studies, the flame heights decrease with increased premixing of the fuel jet, consistent with previous work [2]. Similar to the experiment, the flame height in the simulation decreases by approximately 25% from the $\phi_{\text{jet}} = \infty$ to the $\phi_{\text{jet}} = 6$ flame. However, the flame heights are under-predicted by 10-15% in the simulation as compared to the experiment.

3.2 Effect of air addition on soot volume fraction distribution.

Figure 1 shows that the soot is first detected in the annular region and then develops towards the flame centerline at higher heights above the burner (HAB) for both non-premixed and premixed flames; this trend of soot development is consistent with previous results [10]. However, the location of the maximum f_v changes significantly with premixing. In the non-premixed flame, Fig. 1a shows that the location of peak soot is in the annular region; the peak f_v is approximately 40% higher in annular region as compared to the centerline. In the $\phi_{\text{jet}} = 24$ flame, the peak f_v is approximately 20% higher in the annular region as compared to the centerline. With the increase in premixing, the location of peak f_v shifts from

the flame annular region to the flame centerline. Figures 1e and 1g show that the soot field is relatively uniform in the mid-section of the flame, with a peak f_v of approximately 6 ppm and 5 ppm in the $\phi_{\text{jet}} = 12$ and 6 flames, respectively.

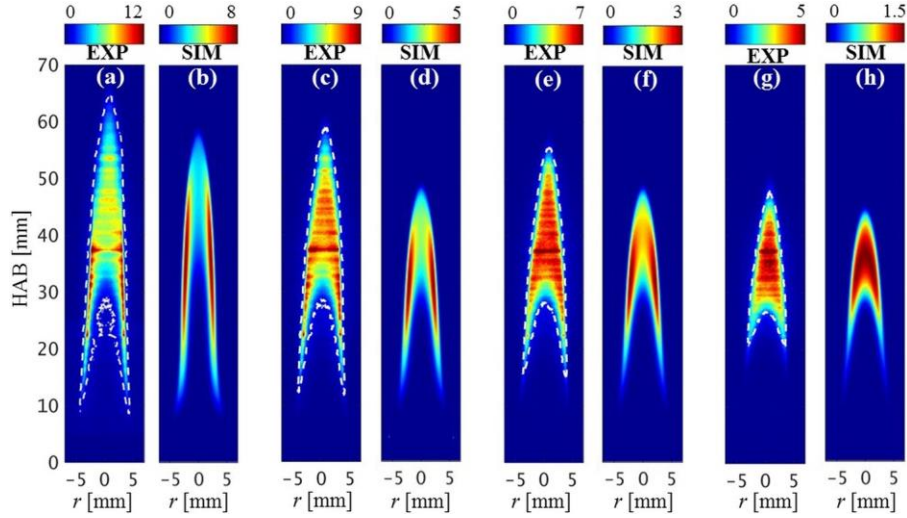


Figure 1: Two dimensional image of the f_v [ppm] for ϕ_{jet} of (a, b) ∞ , (c, d) 24, (e, f) 12, and (g, h) 6.

Comparison of the numerical and experimental results shows that the simulation captures the spatial trends of the soot field. Figures 1b and 1d show that in the $\phi_{\text{jet}} = \infty$ and 24 flames, the peak f_v location is in the annular region, and it transitions to the centerline as the equivalence ratio is reduced. In the non-premixed flame, the peak f_v is 65% higher in the annular region as compared to the centerline. In the $\phi_{\text{jet}} = 6$ flame, the peak f_v is near the centerline, consistent with the experimental results. The qualitative trend of transition of peak f_v from the annular region to the centerline is identical to the previous studies in ethylene flames [5, 10].

Figure 2 shows the comparison of peak f_v against $1/\phi_{\text{jet}}$ in the whole domain and on centerline in the experiment and simulation for all the flames. In both experiment and simulation, the peak f_v decreases with premixing. The peak f_v in the domain decreases by 60% and 80% from $\phi_{\text{jet}} = \infty$ to $\phi_{\text{jet}} = 6$ in experiment and simulation, respectively. The peak centerline f_v decreases by 33% and 45% from $\phi_{\text{jet}} = \infty$ to $\phi_{\text{jet}} = 6$ in experiment and simulation, respectively. The model predicts the percentage decrease in peak f_v due to premixing to be higher in the annular region as compared to the centerline, as in the experiment. On the

centerline, the peak f_v shows a decreasing linear trend with increased premixing; this trend is captured well in the simulation. However, the model over-predicts the percentage decrease in peak f_v due to premixing by approximately 20%. Quantitatively, the peak f_v in the simulation is lower by a factor of 1.3-2.8 as compared to the experiment. A similar level of accuracy by numerical models has been reported in co-flow flame studies [6, 27].

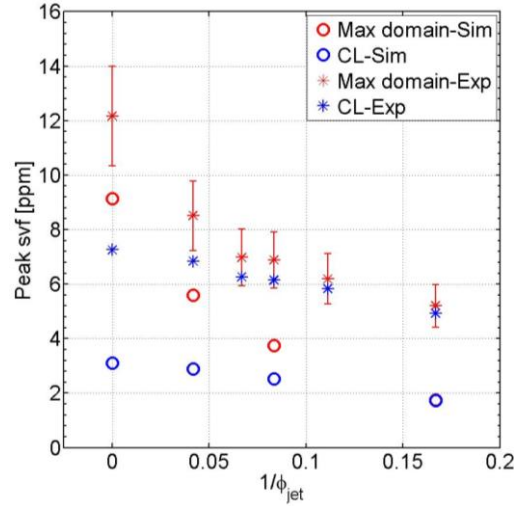


Figure 2: Comparison of peak f_v against $1/\phi_{jet}$ on the centerline and in the whole domain in the experiment and simulation. (Uncertainty bar shows measurement uncertainty of $\pm 15\%$ in f_v)

3.3 Numerical investigation of effects of premixing on soot evolution processes

In order to gain insight into the physical and chemical processes that drive the shift in the peak f_v location from the annular region to the centerline, we compare the nucleation, surface growth, PAH condensation, and oxidation processes amongst the four flames. The details on the models used for these processes can be found in Ref. [24].

3.3.1 Soot nucleation

Figure 3 shows the spatial distribution of PAH dimer concentration (left half of each image) and soot nucleation rate (right half of each image) for the four flames. The maximum values of the scale are shown on the top of each figure. Comparison of Figs. 3a-3d shows that the peak intensity of the nucleation rate shifts from the annular region in the $\phi_{jet} = \infty$ flame to the centerline in the $\phi_{jet} = 6$ flame. This shift in

the location of peak nucleation rate is different than the results of the ethylene flame study by Smooke *et al.* [5]. In the ethylene flame, the authors observed a shift in the soot field, similar to current study, but they did not see a shift in the peak inception rate, which only occurred along the centerline at all nitrogen dilution rates.

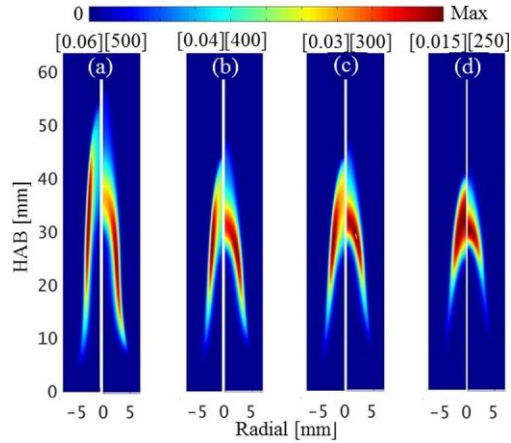


Figure 3: Spatial distribution of the PAH dimer concentration (left half) and nucleation rate [$*10^{-6}$] [1/s] (right half) for ϕ_{jet} : (a) ∞ , (b) 24, (c) 12, and (d) 6. The maximum value of the scale for each subplot are shown on the top of each figures. For example, the maximum value for the left and right half of Fig. 3(a) is 0.06 and 500, respectively.

In the current soot model, the soot nucleation rate is dependent on the local temperature and dimer concentration [24], *i.e.* $\dot{\omega}_{nucl} \propto [T]^{0.5} [DIMER]^2$. Therefore, the shift in the location of peak nucleation rate with premixing could be due to the change in the PAH dimer spatial distribution and/or temperature field. In the current soot model, naphthalene, acenaphthylene, biphenyl, phenanthrene, acephenanthrylene, pyrene, fluoranthene, and cyclopenta[cd]pyrene are the PAH molecules collide to form DIMER [24]. Table 2 reports the peak nucleation, condensation, and surface growth rates along two streamlines: one that passes through maximum f_v in the domain and another on the centerline. At the locations of peak soot nucleation, condensation, and surface growth, the value of the various parameters that affect the soot sub-mechanisms are also reported in Table 2.

Table 2. Maximum value of the parameters affecting nucleation, condensation and surface growth over two streamlines: passes through the centerline and the maximum f_v location.

	Parameter	Max f_v location streamline			Centerline streamline		
		$\phi_{jet} = \infty$	$\phi_{jet} = 6$	Ratio	$\phi_{jet} = \infty$	$\phi_{jet} = 6$	Ratio
Residence time (ms)		115	60	-	108	60	-
Nucleation	$\dot{\omega}_{nucl}$	5.11E-04	3.33E-04	1.53	3.66E-04	3.33E-04	1.10
	T (K)	1530	1580	-	1470	1580	-
	[DIMER]	6.01E-02	7.03E-03	8.55	1.19E-02	7.03E-03	1.69
Condensation	$\dot{\omega}_{cond}$	5.78E-04	7.89E-05	7.33	1.23E-04	7.89E-05	1.56
	T (K)	1570	1670	-	1540	1670	-
	[DIMER]	7.16E-02	1.36E-02	5.26	2.21E-02	1.36E-02	1.63
	Number Density (1/cm ³)	9.40E+15	1.66E+15	5.66	2.98E+15	1.66E+15	1.80
Surface growth	$\dot{\omega}_{surf}$	2.00E-04	6.21E-05	3.22	6.81E-05	6.21E-05	1.10
	k4	3.79E-03	4.66E-03	0.81	1.54E-03	4.66E-03	0.33
	[C2H2]	1.05E+04	1.45E+04	0.72	4.40E+03	1.45E+04	0.30
	r/(1+r)	3.75E-03	6.49E-03	0.58	8.85E-03	6.49E-03	1.36
	Number of active sites (P)	1.640	0.522	3.14	0.683	0.522	1.30

At the peak nucleation location, Table 2 shows that the temperature increases by approximately 50 K from 1530 K in the $\phi_{jet} = \infty$ flame to 1580 K in the $\phi_{jet} = 6$ flame. Due to the square root dependence of nucleation rate on temperature, the temperature increase doesn't have a significant effect on the nucleation rate. However, the dimer concentration decreases by a factor of eight in the $\phi_{jet} = 6$ flame as compared to the $\phi_{jet} = \infty$ flame. The net result is that the dimer concentration has a dominant effect on the nucleation rate in these flames. Figure 3 shows the PAH dimer concentration, which is obtained by using techniques described in Ref. [24]. The comparison of spatial distribution of PAH dimers shows that the location of peak concentration of PAH dimer is in the annular region and near centerline in $\phi_{jet} = \infty$ and 6

flames, respectively. These differences in the PAH dimer distribution among the four flame results in the shift in the location of peak nucleation rate from annular region to centerline due to premixing. Furthermore, the concentration of PAH species decreases with increased premixing, leading to a decrease in the dimer concentration, and therefore, the nucleation rate from the $\phi_{\text{jet}} = \infty$ to the $\phi_{\text{jet}} = 6$ flame. The shift in peak PAH dimer location and decrease in the PAH concentration with premixing is consistent with the observed trends in the PAH-LIF measurements in previous work [2].

Simulations in a closed homogeneous reactor model are used to explore the effects of air addition on the *iso*-octane pyrolysis at constant temperature (1500 K) and pressure (1 atm). Under both non-premixed and partially-premixed conditions ($\phi_{\text{jet}} = 6$), the simulations show that propargyl recombination is the dominant pathway to the formation of A1 (benzene). The alkyl radicals formed from *iso*-octane decomposition react to form *iso*-butene and propene as the major decomposition products [28]. The propene and *iso*-butene can form propadiene [29], which forms the propargyl radical [29]. Subsequently, propargyl leads to benzene formation through self-addition reaction [30]. The rate of formation of benzene is reduced with premixing due to a reduction in propargyl radical mole fraction. The reduction in propargyl radical could be the result of dilution and/or oxidation of C_3H_3 or the radicals that form C_3H_3 by O_2/OH .

3.3.2 Soot growth: PAH condensation and surface reaction

Figure 4 shows the comparison of soot growth rate due to PAH condensation (left half of each image) and the HACA mechanism (right half of each image) for the four flames. The soot growth rates in Fig. 4a-4d show that with increasing premixing, the peak soot growth rate due to both PAH condensation and the HACA mechanism shifts from the annular region in the $\phi_{\text{jet}} = \infty$ flame to the centerline in the $\phi_{\text{jet}} = 6$ flame. Additionally, similar to the soot nucleation rate, the peak growth rates due to PAH condensation and the HACA mechanism decrease by approximately a factor of seven and three, respectively, as premixing is increased.

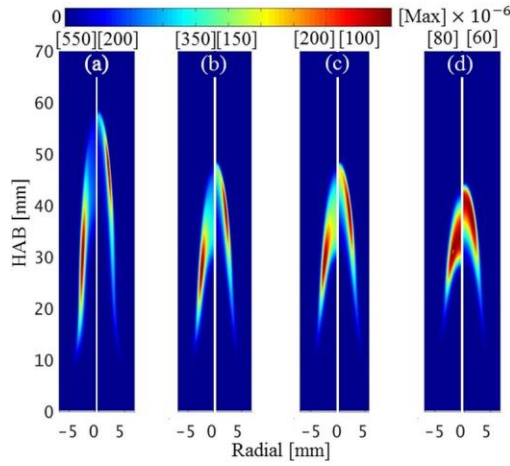


Figure 4: Spatial distribution of the PAH condensation rate [1/s] (left half) and soot surface growth rate [1/s] (right half) for ϕ_{jet} : (a) ∞ , (b) 24, (c) 12, and (d) 6. The maximum value of the scale are shown on the top of each figures.

The condensation and surface growth terms, which are modeled according to Ref. [24], are given by,

$$\dot{\omega}_{cond} \propto [T]^{0.5} [DIMER] \quad (4)$$

$$\dot{\omega}_{surf} \propto k_4 [C_2H_2] P (r/1 + r) \quad (5)$$

where k_4 , $[C_2H_2]$, P , and r are the per-site rate coefficient for acetylene addition, the concentration of acetylene, number of active site on the soot surface, and the ratio of radical to neutral sites on the particle surface, respectively. r is given by

$$r = \frac{k_{1f}[H] + k_{2f}[OH] + k_{3f}}{k_{1b}[H_2] + k_{2b}[H_2O] + k_{3b}[H] + k_4[C_2H_2]} \quad (6)$$

The various rate constants can be found in [20].

The PAH condensation rate depends on the local temperature, PAH dimer concentration, and soot number density. Table 2 shows that with premixing, the temperature increases by 100 K, which could result in an increase in the PAH condensation rate in the $\phi_{jet} = 6$ flame as compared to the $\phi_{jet} = \infty$ flame. However, dimer concentration and soot number density decreases by a factor of five with premixing. The condensation rate decreases with premixing as a result of the decrease in dimer concentration and soot

number density. The dimer concentration decreases with premixing as a result of the decrease in PAH formation in the flame. The soot number density decreases with premixing as a result of the decrease in nucleation rate. The decrease in PAH condensation, in turn, further hampers soot growth. Table 2 shows that the ratio of dimer concentration and soot number density, from $\phi_{\text{jet}} = \infty$ to $\phi_{\text{jet}} = 6$, decreases by approximately a factor of five and two in the whole domain and on centerline, respectively. The higher reduction of dimer concentration and soot number density in the whole domain results in greater reduction of the condensation rate in the annular region as compared to the centerline.

Table 2 shows that several key parameters for surface growth increase with premixing, including k_4 , C_2H_2 concentration, and the ratio of radical to neutral sites on the particle surface. However, the total number of active sites on the soot surface decreases by a factor of three from $\phi_{\text{jet}} = \infty$ to $\phi_{\text{jet}} = 6$. The decrease in the total number of active sites on the soot surface offsets the increase in k_4 , the acetylene concentration, and the ratio of radical to neutral sites on the particle surface in the $\phi_{\text{jet}} = 6$ flame as compared to the $\phi_{\text{jet}} = \infty$ flame. Consequently, the peak soot growth rate due to the HACA mechanism decreases with premixing. Table 2 also shows that the surface growth rate decreases by a greater magnitude in the annular region as compared to the centerline. This greater reduction in soot growth rate leads to a higher percentage decrease of the peak f_v in the annular region as compared to the centerline, as discussed in Section 3.2. Simulations also indicate that the peak location of oxidation shifts from the annular region in the $\phi_{\text{jet}} = \infty$ flame to the centerline in the $\phi_{\text{jet}} = 6$ flame.

3.3.3 Residence time

The total soot produced in a flame is not just a function of the soot production rates, but also the residence time of the soot in the flame. Since the flames are buoyancy driven, the velocities are similar in these flames beyond the exit of the tube [31]. Therefore, the residence time depends on the flame height. Figure 1 shows that the flame height decreases due to premixing. The residence time is calculated by measuring the time for the soot f_v to fall below the cut-off of 0.1 ppm along the two streamlines, along the

flame centerline and the maximum f_v location. Table 2 shows that the residence time is similar along the two streamlines for both flames. As a result, the total residence time available for soot processes decreases by approximately 50 ms in the $\phi_{\text{jet}} = 6$ flame as compared to the $\phi_{\text{jet}} = \infty$ flame. The longer residence time, along with faster soot production processes, result in higher soot growth in the non-premixed flame.

4. Conclusions

In this paper, the effects of premixing on soot formation processes are investigated experimentally and numerically in *iso*-octane co-flow flames. LII results show that the spatial distribution of soot changes in the flames with premixing. As a result of premixing the fuel-jet, the peak soot location shifts from the annular region in the non-premixed flame towards the centerline in the $\phi_{\text{jet}} = 6$ flame. Numerical simulations capture these trends. The peak rate of soot nucleation, condensation, and surface growth processes shift from the annular region towards the centerline with premixing. The soot residence time also decreases in the flame due to premixing. The change in location of peak rates of soot formation processes, along with the decrease in the residence time, result in changes in the soot spatial distribution.

The simulation shows that the location of peak PAH dimer concentration shifts from the annular region in the $\phi_{\text{jet}} = \infty$ flame to the centerline in the $\phi_{\text{jet}} = 6$ flame. This change in PAH dimer distribution results in a shift in the region where soot nucleation and PAH condensation rates peak. Additionally, PAH dimer concentration decreases with increased premixing, leading to a decrease in the soot nucleation rate. The reduction in soot nucleation rate, in turn, reduces soot number density, and therefore, soot surface area available for soot growth processes due to surface reactions and PAH condensation. Furthermore, the reduction in PAH dimer concentration due to premixing also results in a reduction of soot growth due to PAH condensation. The experimental results presented here provide validation quality data to test chemical models for *iso*-octane fuel under both non-premixed and partially-premixed conditions.

Acknowledgements

The experimental work was supported by the Strategic Environmental Research and Development Program (WP-2145) under the direction of Dr. Robin Nissan and Mr. Bruce Sartwell. This work used the

Extreme Science and Engineering Discovery Environment (XSEDE), which is supported by National Science Foundation grant number TG-CTS150017.

References

- [1] Wang, Y., A. Makwana, S. Iyer, M. Linevsky, R.J. Santoro, T.A. Litzinger, and J. O'Connor, *Combust. Flame*, **189** (2018) 443-455.
- [2] Makwana, A., Y. Wang, S. Iyer, M. Linevsky, R.J. Santoro, T.A. Litzinger, and J. O'Connor, *Combust. Flame*, **189** (2018) 456-471.
- [3] Colket, M., T. Edwards, S. Williams, N.P. Cernansky, D.L. Miller, F. Egolfopoulos, P. Lindstedt, K. Seshadri, F.L. Dryer, and C.K. Law. *Development of an experimental database and kinetic models for surrogate jet fuels. 45th AIAA Aerospace Sciences Meeting and Exhibit*. 2007.
- [4] Pitz, W.J., N.P. Cernansky, F.L. Dryer, F. Egolfopoulos, J. Farrell, D. Friend, and H. Pitsch, SAE Technical Paper 2007-01-0175.
- [5] Smooke, M., M. Long, B. Connelly, M. Colket, and R. Hall, *Combust. Flame*, **143**(4) (2005) 613-628.
- [6] Consalvi, J.-L., F. Liu, J. Contreras, M. Kashif, G. Legros, S. Shuai, and J. Wang, *Combust. Flame*, **162**(4) (2015) 1153-1163.
- [7] Khosousi, A., F. Liu, S.B. Dworkin, N.A. Eaves, M.J. Thomson, X. He, Y. Dai, Y. Gao, F. Liu, and S. Shuai, *Combust. Flame*, **162**(10) (2015) 3925-3933.
- [8] Frenzel, I., H. Krause, and D. Trimis, *Energy Procedia*, **120** (2017) 721-728.
- [9] Zeng, M., J. Wullenkord, I. Graf, and K. Kohse-Höinghaus, *Combust. Flame*, **184** (2017) 41-54.
- [10] Santoro, R., H. Semerjian, and R. Dobbins, *Combust. Flame*, **51** (1983) 203-218.
- [11] Chernov, V., Q. Zhang, M.J. Thomson, and S.B. Dworkin, *Combust. Flame*, **159**(9) (2012) 2789-2798.
- [12] Xuan, Y. and G. Blanquart, *Combust. Flame*, **166** (2016) 113-124.
- [13] Xuan, Y. and G. Blanquart, *Combust. Flame*, **160**(9) (2013) 1657-1666.
- [14] Xuan, Y. and G. Blanquart, *Proc. Combust. Inst.*, **35**(2) (2015) 1911-1919.
- [15] Santoro, Robert J., and Christopher R. Shaddix, Taylor & Francis, U.S., (2002) 252-286.
- [16] Dasch, C.J., *Applied Optics*, **31**(8) (1992) 1146-1152.
- [17] Desjardins, O., G. Blanquart, G. Balarac, and H. Pitsch, *J. of Comp. Phys.*, **227**(15) (2008) 7125-7159.
- [18] Herrmann, M., G. Blanquart, and V. Raman, *AIAA journal*, **44**(12) (2006) 2879.
- [19] Savard, B., Y. Xuan, B. Bobbitt, and G. Blanquart, *J. Comp. Phys.*, **295** (2015) 740-769.
- [20] Blanquart, G., P. Pepiot-Desjardins, and H. Pitsch, *Combust. Flame*, **156**(3) (2009) 588-607.
- [21] Raj, A., I.D.C. Prada, A.A. Amer, and S.H. Chung, *Combust. Flame*, **159**(2) (2012) 500-515
- [22] G. Blanquart, available at <<http://www.theforce.caltech.edu/CaltechMech/>>.
- [23] Lapointe, S. and G. Blanquart, *Combust. Flame*, **167** (2016) 294-307.
- [24] Blanquart, G. and H. Pitsch, *Combust. Flame*, **156**(8) (2009) 1614-1626.
- [25] Bisetti, F., G. Blanquart, M.E. Mueller, and H. Pitsch, *Combust. Flame*, **159**(1) (2012) 317-335.
- [26] Gomez, A. and D.E. Rosner, *Combust. Sci. and Tech.*, 1993. **89**(5-6): p. 335-362.
- [27] Saffaripour, M., M. Kholghy, S. Dworkin, and M. Thomson, *Proc. Combust. Inst.*, **34**(1) (2013) 1057-1065.
- [28] Curran, H.J., P. Gaffuri, W. Pitz, and C. Westbrook, *Combust. Flame*, **129**(3) (2002) 253-280.
- [29] McEnally, C.S., D.M. Ciuparu, and L.D. Pfefferle, *Combust. Flame*, **134**(4) (2003) 339-353.
- [30] McEnally, C.S., L.D. Pfefferle, B. Atakan, and K. Kohse-Höinghaus, *Progress in Energy and Combust. Sci.*, **32**(3) (2006) 247-294.
- [31] Santoro, R., T. Yeh, J. Horvath, and H. Semerjian, *Combust. Sci. and Tech.*, **53**(2-3) (1987) 89-115.

Figure captions:

Figure 1: Two dimensional image of the f_v [ppm] for ϕ_{jet} of (a, b) ∞ , (c, d) 24, (e, f) 12, and (g, h) 6.

Figure 2: Comparison of peak f_v against $1/\phi_{jet}$ on the centerline and in the whole domain in the experiment and simulation. (Uncertainty bar shows measurement uncertainty of $\pm 15\%$ in f_v)

Figure 3: Spatial distribution of the PAH dimer concentration (left half) and nucleation rate [$*10^{-6}$] [1/s] (right half) for ϕ_{jet} : (a) ∞ , (b) 24, (c) 12, and (d) 6. The maximum value of the scale for each subplot are shown on the top of each figures. For example, the maximum value for the left and right half of Fig. 3(a) is 0.06 and 500, respectively.

Figure 4: Spatial distribution of the PAH condensation rate [1/s] (left half) and soot surface growth rate [1/s] (right half) for ϕ_{jet} : (a) ∞ , (b) 24, (c) 12, and (d) 6. The maximum value of the scale are shown on the top of each figures.